Chapter 13
Modeling Soft Swimming Robots using Discrete Elastic Rod Method

Weicheng Huang, Zachary Patterson, Carmel Majidi, and M. Khalid Jawed

13.1 Introduction

Recent progress in the field of soft robotics [1] has led to new classes of bio-inspired swimming robots that are largely composed of soft and elastically deformable materials. These include robots powered with hydraulics [2], ionic polymer–metal composites (IPMCs) [3], dielectric elastomer actuators (DEAs) [4], and shape memory alloys (SMAs) [5]. SMA-powered actuators are especially promising for swimming robots since the heat used to activate the SMA can be quickly dissipated by convection through the surrounding water. An example of a soft swimming robot inspired by the seastar is presented in Fig. 13.1. The limbs of the robot are composed of soft silicone elastomer that are embedded with SMA wires. When electrical current is delivered to the wires, they cause the limbs to bend and generate a forward thrust.

There are a variety of computational tools that can be used to model soft robots like the seastar-inspired robot described above. These include reduced-order finite element analysis (FEA) formulations [6–9] as well as 3D representations using voxel-based discretization [10, 11]. Recently, there has been interest in modeling soft robots as a combination of slender soft appendages using elastic rod theory [12–14]. When combined with discrete differential geometry (DDG) numerical tools used within the computer graphics community, these rod theories can be used to achieve rapid simulation runtimes.

W. Huang · M. K. Jawed
Mechanical and Aerospace Engineering, University of California, Los Angeles, CA, USA
e-mail: khalidjm@seas.ucla.edu

Z. Patterson · C. Majidi (✉)
Mechanical Engineering, Carnegie Mellon University, Pittsburgh, PA, USA
e-mail: cmajidi@andrew.cmu.edu

D. A. Paley, N. M. Wereley (eds.), *Bioinspired Sensing, Actuation, and Control in Underwater Soft Robotic Systems*, https://doi.org/10.1007/978-3-030-50476-2_13

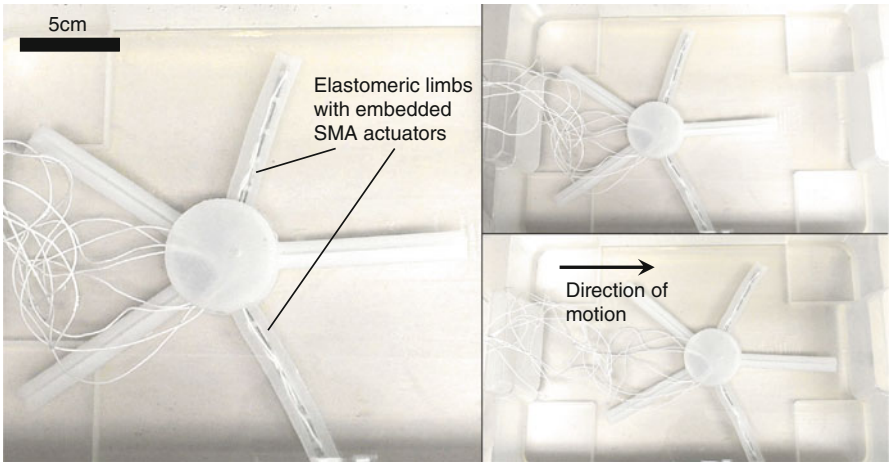

Fig. 13.1 SMA-powered seastar-inspired soft robot

The DDG-based approach to simulation has been used to model elastic slender structures, e.g., rods [15–17], ribbons [18], plates [19], shells [20], X-shells [21], viscous threads [17, 22], and viscous sheets [23]. The method of discrete elastic rods (DER) is emerging as an especially popular tool for rapid simulation of engineered systems composed of slender filamentary structures. Goldberg et al. used a 2D version of DER to simulate a crawling, caterpillar-inspired soft robot in which each robot segment was modeled as an elastic rod element [24].

This chapter shows how DER can be used to simulate seastar-inspired soft swimming robots composed of radiating elastic limbs that flap in response to actuator stimulation. Figure 13.2 presents several snapshots of a seastar-inspired soft robot moving through a prescribed regular pentagon trajectory from simulations. Here, the actuated limbs are highlighted as blue, and the corresponding actuating sequence of the presented trajectory is in Fig. 13.7b. Our analysis is limited to two dimensions, although it can be generalized into 3D as detailed in [15], which presents a comprehensive description of the DER formulation and its application to robotics modeling. We begin with a brief background on DER in Sect. 13.2, followed by an overview of the mathematical formulation used to describe the kinematics, elastic energies, and time-marching scheme of the rod system in Sect. 13.3. Section 13.4 applies this model to simulate the dynamics of a robot composed of five radiating limbs moving in a fluid. Finally, concluding remarks and avenues for future research are presented in Sect. 13.5.

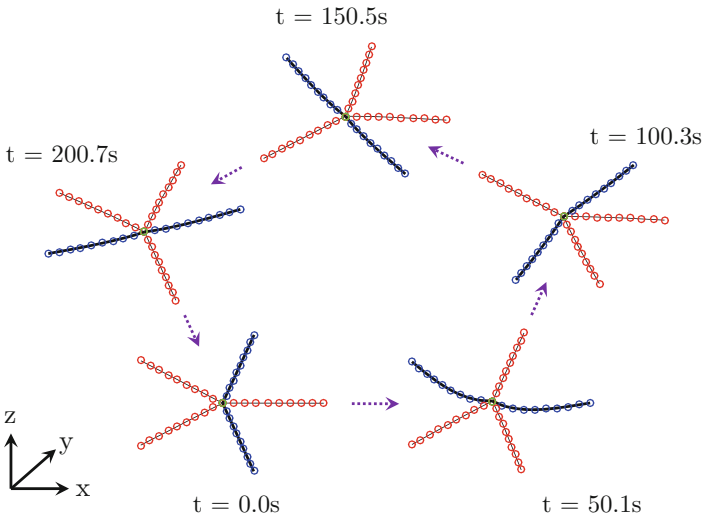

Fig. 13.2 DER-based simulation of a seastar-inspired soft robot following a pentagonal trajectory. The blue bold lines are the actuated limbs

13.2 Background

Kirchhoff introduced a celebrated model for elastic rods in 1859 [25]. A recent and related development in the mechanics of elastic rods came in 2008 with the introduction of discrete elastic rods (DER) [16, 17]—a computationally efficient algorithm that can seamlessly capture the geometrically nonlinear dynamics of elastic rods. Although the method was originally introduced by the computer graphics community, it has been successfully employed in the context of mechanical engineering problems since 2014 [26]. The original DER papers [16, 17] are fairly short in length, yet packed with advanced concepts from discrete differential geometry. A detailed exposition of this method is presented in [15] and generalizations of this modeling approach have been developed for plates [19], shells [20], ribbons [18], and gridshells [21].

For many soft robotic systems, DER is capable of much faster computational speeds than more conventional modeling techniques. This improvement is because the subcomponents of the robot are treated as 1D elements (capable of deformation in two- or three-dimensions) rather than volumetric 3D bodies. The reduction in dimensionality allows for the system of partial differential equations typically used to model 3D elastic bodies to be replaced with a much simpler system of ordinary differential equations. With the analytical formulation of energy variation (related to elastic force) and second variation (known as the Hessian matrix), the equations of motion of the dynamic system can be implicitly updated with a larger time-marching step. For some soft robotic systems, like the seastar-inspired robot studied here, locomotion can be accurately simulated using a reasonable temporal–spatial

discretization in faster than real time. That is, the time required on a single thread of a standard CPU to perform the simulation is faster than the wall-clock time it would take for the robot to perform the physical motion, which is a first step towards a major challenge, i.e., developing online robot controllers, in soft robotic engineering.

13.3 Discrete Elastic Rod Method

Each limb of the soft robot is treated as a planar elastic rod (cf. elastic beam) that bends in the x–y plane. In the discrete setting of DER shown schematically in Fig. 13.3, the rod centerline is discretized into N nodes: $\mathbf{x}_0, \ldots, \mathbf{x}_{N-1}$, where $\mathbf{x}_i \equiv [x_i, \ y_i]^T$, superscript T denotes the transposition operation, and $0 \leq i \leq N-1$, such that the total degree of freedom (DOF) vector is size of $2N$,

$$\mathbf{q} = [x_0, y_0, x_1, y_1, \ldots, x_{N-1}, y_{N-1}]^T. \tag{13.1}$$

This space discretization results into $N-1$ edge vectors: $\mathbf{e}^0, \ldots, \mathbf{e}^{N-2}$, where $\mathbf{e}^i = \mathbf{x}_{i+1} - \mathbf{x}_i$, and $0 \leq i \leq N-2$. Hereafter, we use subscripts to denote quantities associated with nodes, e.g., $\mathbf{x}_i$, and superscripts when associated with edges, e.g., $\mathbf{e}^i$. Based on this kinematic representation, the remainder of this section discusses the formulation of elastic energies, elastic forces, and the time-stepping procedure of the rod system.

An elastic rod is modeled as a mass–spring system, with a lumped mass at each node. Associated with each node and edge is a discrete bending and stretching energy, respectively. In the case of a 3D rod, we would also have to account for the elastic twisting energy and related rotational inertia. For a rod with a constant Young's modulus E, cross-section area A, and second moment of inertia I, the elastic stretching energy associated with the ith edge is

$$E_s^i = \frac{1}{2} EA \left(\epsilon^i\right)^2 \left\|\bar{\mathbf{e}}^i\right\|, \tag{13.2}$$

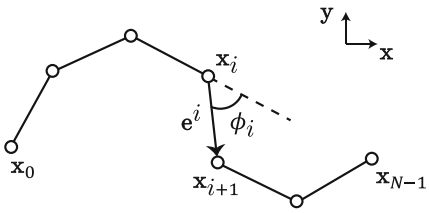

Fig. 13.3 Schematic of a discrete rod in 2D

where $\epsilon^i = \|\mathbf{e}^i\|/\|\bar{\mathbf{e}}^i\| - 1$ is the axial strain of the ith edge, and notation with the bar on top indicates the quantity is evaluated in the undeformed configuration, e.g., $\|\bar{\mathbf{e}}^i\|$ is the undeformed length of the ith edge.

The bending energy of the ith node is measured by the misalignment between two consecutive edges $\{\mathbf{e}^{i-1}, \mathbf{e}^i\}$, i.e.,

$$E_{b,i} = \frac{1}{2} EI(\kappa_i - \bar{\kappa}_i)^2 \Delta l_i, \tag{13.3}$$

where $\kappa_i = 2\tan(\phi_i/2)/\Delta l_i$ is the discrete curvature at the ith node and $\Delta l_i = (\|\bar{\mathbf{e}}^{i-1}\| + \|\bar{\mathbf{e}}^i\|)/2$ is its Voronoi length. The turning angle ϕ_i is

$$\phi_i = \tan^{-1} \frac{\left(\mathbf{e}^{i-1} \times \mathbf{e}^i\right) \cdot \hat{\mathbf{n}}_z}{\mathbf{e}^{i-1} \cdot \mathbf{e}^i}, \tag{13.4}$$

where $\hat{\mathbf{n}}_z$ is the unit vector along the z-axis, i.e., the numerator on the right-hand side is the z-component of the cross-product between $\mathbf{e}^{i-1}$ and $\mathbf{e}^i$. Note that ϵ^i, κ_i, and ϕ_i represent the finite difference approximations of stretch, curvature, and turning angle.

The total potential energy of the rod system is obtained by summing the elastic stretching energies over all the edges and bending energies over all the nodes (except the first and the last nodes where the bending energies are always zero), i.e.,

$$E = \sum_{i=0}^{N-2} E_s^i + \sum_{i=1}^{N-2} E_{b,i}. \tag{13.5}$$

Next, the internal elastic force vector $\mathbf{F}^{\text{int}}$ is the negative gradient of the total potential energy:

$$\mathbf{F}^{\text{int}} = -\frac{\partial E}{\partial \mathbf{q}}. \tag{13.6}$$

Specifically, the non-zero force component of the ith node, $[F_{2i}^{\text{int}},\ F_{2i+1}^{\text{int}}]^T$, is only related to five neighboring energy terms: E_s^{i-1}, E_s^i, $E_{b,i-1}$, $E_{b,i}$, and $E_{b,i+1}$. We have

$$F_{2i}^{\text{int}} = -\frac{\partial}{\partial x_i}\left(E_s^{i-1} + E_s^i + E_{b,i-1} + E_{b,i} + E_{b,i+1}\right) \qquad \text{and} \tag{13.7a}$$

$$F_{2i+1}^{\text{int}} = -\frac{\partial}{\partial y_i}\left(E_s^{i-1} + E_s^i + E_{b,i-1} + E_{b,i} + E_{b,i+1}\right) \tag{13.7b}$$

Next, we turn to the formulation of the external force vector. The external force is comprised of the force from the external environment, e.g., gravity, damping force from a viscous medium [27], or the actuation force from an external electromagnetic

field [28]. Here, we consider the hydrodynamic force from fluid experienced by soft robotic limbs as the external force in our numerical framework. The discretized version of a fluid drag force applied on the ith node is [29, 30]

$$\mathbf{F}_i^{\text{ext}} = -\frac{1}{2}\rho_f C_d D \|\mathbf{v}_i\| \mathbf{v}_i \Delta l_i, \tag{13.8}$$

where ρ_f is the density of fluid medium, $D = 2r_0$ is the diameter of the rod, C_d is the drag coefficient, and $\mathbf{v}_i \equiv [\dot{x}_i, \dot{y}_i]^T$ is the relative velocity of the ith node and fluid. The external force vector (size $2N$) on the entire rod is $\mathbf{F}^{\text{ext}} = \left[\mathbf{F}_0^{\text{ext}}, \mathbf{F}_1^{\text{ext}}, \ldots, \mathbf{F}_{N-1}^{\text{ext}}\right]^T$.

Finally, we discuss the time-marching scheme. We update the equations of motion of a discrete rod system by a first-order, implicit Euler method, because of its unconditional convergence and numerical stability [31]. We solve the following $2N$ equation of motions and update the DOF vector $\mathbf{q}$ and its velocity (time derivative of DOF) $\mathbf{v} = \dot{\mathbf{q}}$ from time step t_k to $t_{k+1} = t_k + h$ (h is the time step size) based on the following statement of force balance:

$$\mathbf{f} \equiv \mathbb{M}\frac{[\mathbf{q}(t_{k+1}) - \mathbf{q}(t_k) - h\mathbf{v}(t_k)]}{h^2} - \mathbf{F}^{\text{int}}(t_{k+1}) - \mathbf{F}^{\text{ext}}(t_{k+1}) = \mathbf{0}, \tag{13.9}$$

where $\mathbb{M}$ is the diagonal mass matrix comprised of the lumped masses, $\mathbf{F}^{\text{int}}$ is the internal elastic force given by Eqs. (13.6) and (13.14), $\mathbf{F}^{\text{ext}}$ is the external force formulated in Eq. (13.8), and t_k denotes evaluation of the quantity at time t_k.

We use the Newton–Raphson method to solve this set of nonlinear equations of motion. At each time step t_{k+1}, we first guess a new solution on the basis of the previous state, i.e.,

$$\mathbf{q}^{(1)}(t_{k+1}) = \mathbf{q}(t_k) + h\mathbf{v}(t_k). \tag{13.10}$$

Then, we optimize the solutions by gradient decent, such that the new solution at the $(k+1)$th step is

$$\mathbf{q}^{(n+1)}(t_{k+1}) = \mathbf{q}^{(n)}(t_{k+1}) - \mathbb{J}^{(n)} \backslash \mathbf{f}^{(n)}, \tag{13.11}$$

where $\mathbb{J}$ is the Jacobian matrix associated with Eq. (13.9),

$$\mathbb{J} \equiv \frac{\partial \mathbf{f}}{\partial \mathbf{q}} = \frac{1}{h^2}\mathbb{M} + \frac{\partial^2 E}{\partial \mathbf{q} \partial \mathbf{q}} - \frac{\partial \mathbf{F}^{\text{ext}}}{\partial \mathbf{q}}. \tag{13.12}$$

A detailed formulation of the Hessian matrix associated with the elastic energy, i.e., the second term $\partial^2 E/\partial \mathbf{q}^2$ in Eq. (13.12), is in [17]. The Jacobian associated with the external force, $\frac{\partial \mathbf{F}^{\text{ext}}}{\partial \mathbf{q}}$, can be re-written as $\frac{1}{h}\frac{\partial \mathbf{F}^{\text{ext}}}{\partial \mathbf{v}}$ and trivially computed from Eq. (13.8). Importantly, the Jacobian $\mathbb{J}$ is a banded matrix and the time complexity of this algorithm is $O(N)$ for a single rod system (the computational time linearly

scales with the number of node). This computational efficiency has motivated its application in the animation industry (e.g., hair simulation for movies) as well as its adoption in mechanical engineering.

13.4 Simulation

Here, the main steps of the algorithm for modeling the dynamics of a soft swimming robot with the DER method are outlined below. We first introduce the geometric discretization of the seastar-inspired soft robot composed of a number of SMA-based actuators. Next, the modeling of the actuators is discussed, followed by a discussion of the locomotion of the seastar-inspired soft robot in two special cases: a straight path and a regular pentagonal trajectory. Finally, the computational efficiency of the DER-based numerical framework is detailed.

In Fig. 13.4a, we model the seastar-inspired soft robot with five planar elastic rods connected at the center point, $\mathbf{x}_0 \equiv [x_0,\ y_0]^T$. Each limb, with arc length $L = 0.1\,\text{m}$, is discretized into N nodes and $N-1$ edges. In the current study, we choose $N = 10$, resulting in an edge length of $\Delta L \approx 1.11\,\text{cm}$. As all five limbs share the center node, $\mathbf{x}_0$, the total number of nodes in the soft robot system is $n = 5 \times N - 4$. The ith node on jth limb is denoted as $\mathbf{x}_{\{j,i\}}$. The material properties used in this numerical study are as follows: Young's modulus $E = 1\text{MPa}$, material density $\rho_m = 1000\,\text{kg/m}^3$, fluid density $\rho_f = \rho_m$ (neutrally buoyant), rod radius $r_0 = 1.6$ mm (and, therefore, second moment of inertia $I = \pi r_0^4/4$ and diameter $D = 2r_0$), and drag coefficient $C_d = 1.0$.

Besides the bending and stretching energies formulated in the DER method for each limb, the bending energy at the center node requires special treatment. As shown in Fig. 13.4b, the bending energy between the first limb and second limb at the center node is

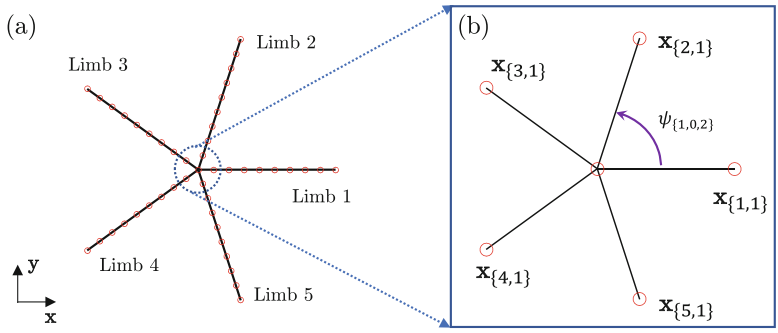

Fig. 13.4 (**a**) Geometric discretization of seastar-inspired soft robot. (**b**) Zoomed-in description of the center point

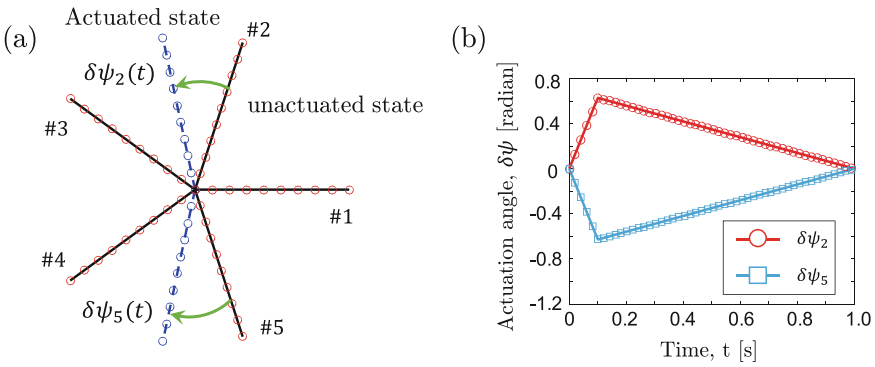

Fig. 13.5 (**a**) Actuated and unactuated state of seastar-inspired robot. (**b**) Actuation signal of #2 and #5 limbs: rotating angle, $\delta\psi$, as a function of time during one actuation cycle

$$E_{b,\{1,0,2\}} = \frac{1}{2} EI \left(\kappa_{\{1,0,2\}} - \bar{\kappa}_{\{1,0,2\}}\right)^2, \tag{13.13}$$

where $\kappa_{\{1,0,2\}}$ is measured by the angle between the first limb and second limb, $\psi_{\{1,0,2\}}$. Similarly, there are four more components to the bending energy at the center node associated with the angles $\psi_{\{2,0,3\}}$, $\psi_{\{3,0,4\}}$, $\psi_{\{4,0,5\}}$, and $\psi_{\{5,0,1\}}$. Overall, the total elastic energy of seastar-inspired soft robot system is

$$E_{\text{total}} = \sum_{j=1}^{5} \left[\left(\sum_{i=0}^{N-2} E_s^i \right)_j + \left(\sum_{i=1}^{N-2} E_{b,i} \right)_j \right] \tag{13.14a}$$

$$+ E_{b,\{1,0,2\}} + E_{b,\{2,0,3\}} + E_{b,\{3,0,4\}} + E_{b,\{4,0,5\}} + E_{b,\{5,0,1\}}. \tag{13.14b}$$

Its first gradient (negative internal force) and second gradient (Hessian matrix) can be analytically formulated in a manner similar to common applications of the DER methods.

Actuation is incorporated into the simulation by varying the natural curvature between two neighboring limbs, e.g., $\bar{\kappa}_{\{1,0,2\}}$ in Eq. (13.13), with time. This variation is measured through characterization of a single SMA-powered actuator, as described next. The electrically activated SMA wire enables rapid transition between the unactuated state and the actuated state [32, 33]. Assume the limbs can rotate by a certain angle as a function of time during the actuating–cooling process, e.g., #2 rotates by an angle $\delta\psi_2(t)$ relative to the rest of the system, as shown in Fig. 13.5a. We define anti-clockwise rotation as positive and clockwise rotation as negative.

Usually, experimental characterization of an actuator can be used to get the actuation function, e.g., $\delta\psi_2(t)$. Here, for simplicity, we assume a piecewise linear function, shown in Fig. 13.5b, to describe the actuated and cooling state. We actuated limbs #2 and #5 simultaneously for the straight locomotion along X-

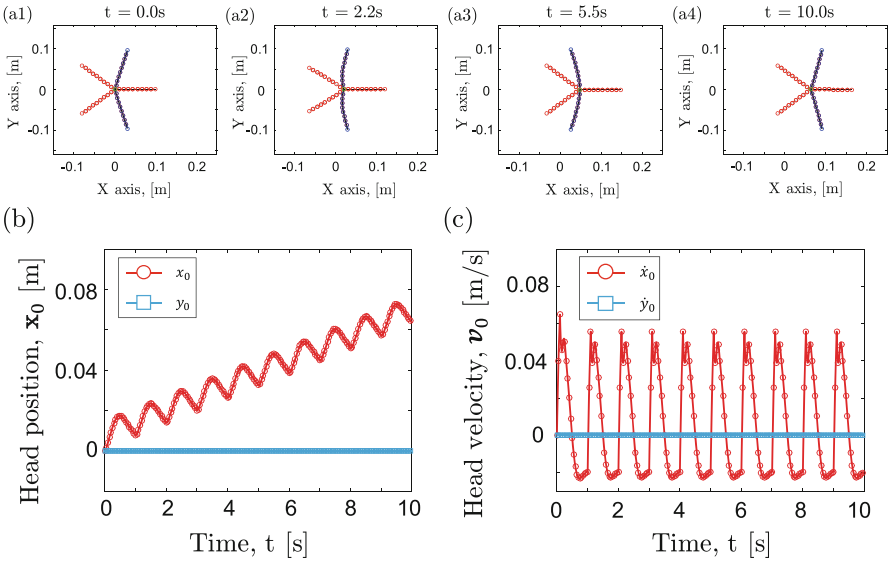

Fig. 13.6 (**a1**)–(**a4**) Snapshots of swimming seastar-inspired robot at different time steps, $t = 0.0\,\text{s}$, $2.2\,\text{s}$, $5.5\,\text{s}$, and, $10.0\,\text{s}$. (**b**) Head node position as a function of time. (**c**) Head node velocity as a function of time

axis, and the maximum actuation angle is $\pi/5$, which is half of the angle between two neighboring limbs in the undeformed configuration. The actuation period in Fig. 13.5b is $\Delta t_0 = 1.0\,\text{s}$, with actuating time $\Delta t_1 = 0.1\,\text{s}$ and cooling time $\Delta t_2 = 0.9\,\text{s}$.

By symmetrically actuating limbs #2 and #5 with the input shown in Fig. 13.5b, this bio-inspired swimming robot can move forward along the X-axis. In Fig. 13.6a1–a4, we show multiple snapshots of the seastar-inspired soft robot swimming in water at various time steps, $t \in \{0.0, 2.2, 5.5, 10.0\}\,\text{s}$. We observe that the robot swims forward during the actuating phase, but moves slightly backward in the cooling state. Overall, the net motion of the robot is forward over an entire cycle. Figs. 13.6b,c show the center node position and velocity, respectively, as functions of time over 10 actuation periods. Because of the symmetry of geometric and actuating conditions, this bio-inspired soft robot has no displacement or velocity components along the Y-axis.

Next, we show a piecewise-linear trajectory of the robot swimming in a fluid medium. The soft robot can follow a straight trajectory along one limb by actuating the two neighboring limbs next to it, e.g., the soft robot can swim along X-axis (the direction of limb #1) by actuating limbs #2 and #5, as discussed in the previous case. A complex nonlinear trajectory, on the other hand, can be achieved by combining multiple straight trajectories that are not parallel. In Fig. 13.2, we provide some snapshots of a seastar-inspired soft robot moving along a prescribed regular pentagonal trajectory, i.e., a closed path that combines five straight trajectories.

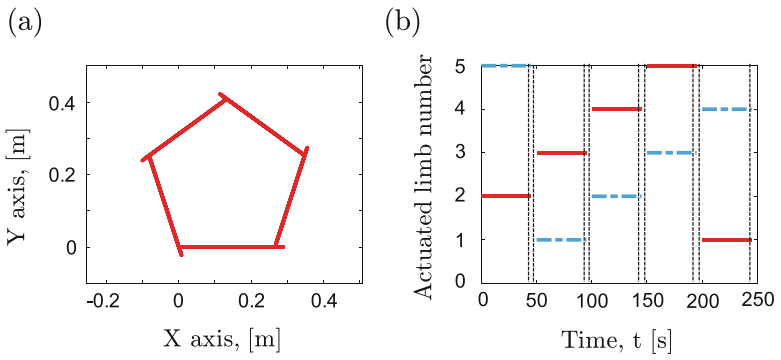

Fig. 13.7 (**a**) Regular pentagon trajectory of seastar-inspired soft robot. (**b**) Actuation input signal for regular pentagon trajectory. Blue dashed line: negative rotating actuation; red solid line: positive rotating actuation

Fig. 13.8 Trajectories of seastar-inspired soft robot when actuating through different combinations of limbs over 10 actuation periods

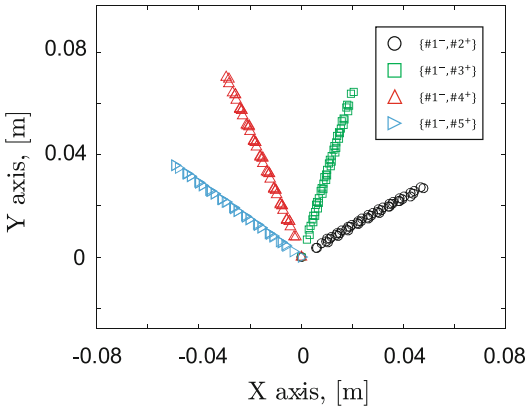

Figure 13.7a shows the trajectory traced by the center node. Here, we actuated two limbs at a time for each straight line segment. For the presented pentagonal trajectory in the current study, the actuation sequence of the limbs is

$$\{2, 5\}\,;\ \{1, 3\}\,;\ \{2, 4\}\,;\ \{3, 5\}\,;\ \{1, 4\}\,, \tag{13.15}$$

as shown in Fig. 13.7b, and the actuating function for each limb is in Fig. 13.5b. During each straight path, we actuated two specific limbs in Eq. (13.15) for 45 s, then left the limbs unactuated for 5 s in order to bring the robot to a complete stop. This way, we maintained the same initial conditions for each straight component of the pentagonal trajectory.

Previous investigations mainly focus on a specific actuating condition. Here, exploiting the efficiency and robustness of our simulator, we perform different actuating combinations of soft limbs. In Fig. 13.8, we plot the trajectories of the seastar-inspired soft robot with different actuated limbs, i.e.,

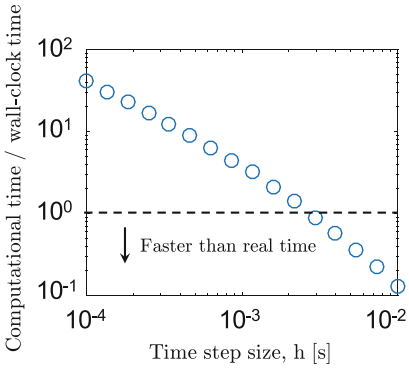

Fig. 13.9 The ratio between computational time and wall-clock time as a function of time step size, h, with a fixed number of vertices, $n = 46$

$\{1^-, 2^+\}$, $\{1^-, 3^+\}$, $\{1^-, 4^+\}$, $\{1^-, 5^+\}$, over 10 actuation periods. Here, positive indicates anti-clockwise rotation and negative indicates clockwise rotation, similar to the previous study. The seastar-inspired soft robot always moves along the bisector of the two actuated limbs, while the translation distance is different. The maximum translation is obtained when actuating limbs #1 and #4 simultaneously, whereas the actuating combination of limbs #1 and #2 has a lower efficiency. Overall, any desired nonlinear trajectory can be fitted by a zig-zag path comprised of some simple straight lines as described above.

Finally, we highlight the computational efficiency of the DER-based soft robotic simulation. For the case of the seastar-inspired swimmer, this numerical framework can achieve real-time simulation speed in which the time required to perform the computation is equal to or faster than the duration of the physical motion being modeled. In Fig. 13.9, with a fixed number of nodes, $n = 46$, the computational time linearly scales with time step size, h. The simulations ran on a single thread of AMD Ryzen 1950X CPU @ 3.4 GHz. The simulator can run faster than real time when the time step size $h \gtrsim 3.0$ ms. Numerical issues associated with large step size appear at $h \gtrsim 20$ ms.

13.5 Conclusion

We have introduced a computational framework to study the dynamics of a seastar-inspired soft robot that is adapted from methods popular in the computer graphics community. This numerical framework integrates elasticity of slender structures, actuation of shape memory alloy, and hydrodynamic loading for fluid–structure interaction, to achieve fast prediction of the motion of seastar-inspired soft robot swimming in a fluid medium. In particular, the DDG-based method presented here can quantitatively predict the robot's motion while running faster than real time on one thread of a contemporary desktop processor. The computational efficiency of this method makes it ideally suited for algorithms that iterate over a wide

variety of parameters in order to select a robot with optimized design. Moving forward, it would be interesting to apply this method to simulate limbed locomotion of soft robots in 3D. This includes the untethered quadruped in [33] as well as the soft SMA-powered robots presented in [34]. Future efforts could also explore the development of a data-driven trajectory planning algorithm for the motion control of bio-inspired soft robots. Such an algorithm would combine rapid, DDG-based simulation of robots with training data for mechanical and fluid–structure interactions obtained from empirical measurements and sensor feedback.

Acknowledgments The authors gratefully acknowledge support from the Office of Naval Research (award #N00014-17-1-2063; Program Manager: Dr. Tom McKenna).

References

1. S.I. Rich, R.J. Wood, C. Majidi, Untethered soft robotics. Nature Electron. **1**(2), 102 (2018)
2. R.K. Katzschmann, A.D. Marchese, D. Rus, Hydraulic autonomous soft robotic fish for 3d swimming, in *Experimental Robotics* (Springer, New York, 2016), pp. 405–420
3. X. Tan, D. Kim, N. Usher, D. Laboy, J. Jackson, A. Kapetanovic, J. Rapai, B. Sabadus, X. Zhou, An autonomous robotic fish for mobile sensing, in *Proceedings of the 2006 IEEE/RSJ International Conference on Intelligent Robots and Systems* (IEEE, New York, 2006), pp. 5424–5429
4. T. Li, G. Li, Y. Liang, T. Cheng, J. Dai, X. Yang, B. Liu, Z. Zeng, Z. Huang, Y. Luo, et al., Fast-moving soft electronic fish. Sci. Adv. **3**(4), e1602045 (2017)
5. M.D. Bartlett, N. Kazem, M.J. Powell-Palm, X. Huang, W. Sun, J.A. Malen, C. Majidi, High thermal conductivity in soft elastomers with elongated liquid metal inclusions. Proc. Natl. Acad. Sci. **114**(9), 2143–2148 (2017)
6. C. Duriez, Control of elastic soft robots based on real-time finite element method, in *Proceedings of the 2013 IEEE International Conference on Robotics and Automation* (IEEE, New York, 2013), pp. 3982–3987
7. G. Runge, A. Raatz, A framework for the automated design and modelling of soft robotic systems. CIRP Annals **66**(1), 9–12 (2017)
8. O. Goury, C. Duriez, Fast, generic, and reliable control and simulation of soft robots using model order reduction. IEEE Trans. Robot. **34**(6), 1565–1576 (2018)
9. J. Chenevier, D. González, J.V. Aguado, F. Chinesta, E. Cueto, Reduced-order modeling of soft robots. PloS One **13**(2), e0192052 (2018)
10. J. Hiller, H. Lipson, Dynamic simulation of soft multimaterial 3d-printed objects. Soft Robot. **1**(1), 88–101 (2014)
11. N. Cheney, J. Bongard, H. Lipson, Evolving soft robots in tight spaces, in *Proceedings of the 2015 annual conference on Genetic and Evolutionary Computation* (ACM, New York, 2015), pp. 935–942
12. X. Zhou, C. Majidi, O.M. O'Reilly, Soft hands: an analysis of some gripping mechanisms in soft robot design. Int. J. Solids Struct. **64**, 155–165 (2015)
13. S. Grazioso, G. Di Gironimo, B. Siciliano, A geometrically exact model for soft continuum robots: the finite element deformation space formulation. Soft Robot. **6**(6), 790–811 (2018)
14. F. Renda, F. Giorgio-Serchi, F. Boyer, C. Laschi, J. Dias, L. Seneviratne, A unified multi-soft-body dynamic model for underwater soft robots. Int. J. Robot. Res. **37**(6), 648–666 (2018)
15. M.K. Jawed, A. Novelia, O.M. O'Reilly, *A primer on the Kinematics of Discrete Elastic Rods*. Springer Briefs in Applied Sciences and Technology (Springer, Berlin, 2018)

16. M. Bergou, M. Wardetzky, S. Robinson, B. Audoly, E. Grinspun, Discrete elastic rods. ACM Trans. Graph. **27**(3), 63 (2008)
17. M. Bergou, B. Audoly, E. Vouga, M. Wardetzky, E. Grinspun, Discrete viscous threads. ACM Trans. Graph. **29**(4), 116 (2010)
18. Z. Shen, J. Huang, W. Chen, H. Bao, Geometrically exact simulation of inextensible ribbon, in *Computer Graphics Forum*, vol. 34 (Wiley, New York, 2015), pp. 145–154
19. D. Baraff, A. Witkin, Large steps in cloth simulation, in *Proceedings of the 25th Annual Conference on Computer Graphics and Interactive Techniques* (ACM, New York, 1998), pp. 43–54
20. E. Grinspun, A.N. Hirani, M. Desbrun, P. Schröder, Discrete shells, in *Proceedings of the 2003 ACM SIGGRAPH/Eurographics Symposium on Computer Animation* (Eurographics Association, Aire-la-Ville, 2003), pp. 62–67
21. J. Panetta, M. Konaković-Luković, F. Isvoranu, E. Bouleau, M. Pauly, X-shells: a new class of deployable beam structures. ACM Trans. Graphics (TOG) **38**(4), 83 (2019)
22. B. Audoly, N. Clauvelin, P.-T. Brun, M. Bergou, E. Grinspun, M. Wardetzky, A discrete geometric approach for simulating the dynamics of thin viscous threads. J. Comput. Phys. **253**, 18–49 (2013)
23. C. Batty, A. Uribe, B. Audoly, E. Grinspun, Discrete viscous sheets, in *ACM Transactions on Graphics*, vol. 31 (ACM, New York, 2012), p. 113
24. N.N. Goldberg, X. Huang, C. Majidi, A. Novelia, O.M. O'Reilly, D.A. Paley, W.L. Scott, On planar discrete elastic rod models for the locomotion of soft robots. Soft Robot. **6**(5), 595–610 (2019)
25. G. Kirchhoff, Ueber das gleichgewicht und die bewegung eines unendlich dünnen elastischen stabes. J. Reine. Angew. Math. **56**, 285–313 (1859)
26. M.K. Jawed, F. Da, J. Joo, E. Grinspun, P.M. Reis, Coiling of elastic rods on rigid substrates. Proc. Natl. Acad. Sci. **111**(41), 14663–14668 (2014)
27. M.K. Jawed, N.K. Khouri, F. Da, E. Grinspun, P.M. Reis, Propulsion and instability of a flexible helical rod rotating in a viscous fluid. Phys. Rev. Lett. **115**(16), 168101 (2015)
28. L. Zhang, J.J. Abbott, L. Dong, K.E. Peyer, B.E. Kratochvil, H. Zhang, C. Bergeles, B.J. Nelson, Characterizing the swimming properties of artificial bacterial flagella. Nano Lett. **9**(10), 3663–3667 (2009)
29. Y. Modarres-Sadeghi, M. Païdoussis, C. Semler, A nonlinear model for an extensible slender flexible cylinder subjected to axial flow. J. Fluids Struct. **21**(5–7), 609–627 (2005)
30. M. Mallick, A. Kumar, N. Tamboli, A. Kulkarni, P. Sati, V. Devi, S. Chandar, Study on drag coefficient for the flow past a cylinder. Int. J. Civil Eng. Res. **5**(4), 301–306 (2014)
31. W. Huang, M.K. Jawed, Newmark-beta method in discrete elastic rods algorithm to avoid energy dissipation. J. Appl. Mech. **86**(8), 084501 (2019)
32. X. Huang, K. Kumar, M.K. Jawed, A. Mohammadi Nasab, Z. Ye, W. Shan, C. Majidi, Highly dynamic shape memory alloy actuator for fast moving soft robots. Adv. Mater. Technol. **4**(4), 1800540 (2019)
33. X. Huang, K. Kumar, M. Jawed, Z. Ye, C. Majidi, Soft electrically actuated quadruped (SEAQ)-integrating a flex circuit board and elastomeric limbs for versatile mobility. IEEE Robot. Autom. Lett. **4**(3), 2415-2422 (2019)
34. X. Huang, K. Kumar, M.K. Jawed, A.M. Nasab, Z. Ye, W. Shan, C. Majidi, Chasing biomimetic locomotion speeds: Creating untethered soft robots with shape memory alloy actuators. Sci. Robot. **3**(25), 7557 (2018)